Thin Solid Films 589 (2015) 303–308

Contents lists available at ScienceDirect

Thin Solid Films

journal homepage: www.elsevier.com/locate/tsf

Atomic layer deposition TiO_2 coated porous silicon surface: Structural characterization and morphological features

Igor Iatsunskyi [a,b,*], Mariusz Jancelewicz [a], Grzegorz Nowaczyk [a], Mateusz Kempiński [a,c], Barbara Peplińska [a,d], Marcin Jarek [a], Karol Załęski [a], Stefan Jurga [a,d], Valentyn Smyntyna [b]

[a] NanoBioMedical Centre, Adam Mickiewicz University, 85 Umultowska str., 61-614, Poznan, Poland
[b] Department of Experimental Physics, Odessa National I.I. Mechnikov University, 42, Pastera str., 65023 Odessa, Ukraine
[c] Faculty of Physics, Adam Mickiewicz University, Umultowska 85, 61-614 Poland
[d] Department of Macromolecular Physics, Adam Mickiewicz University, Umultowska 85, 61-614 Poznan, Poland

ARTICLE INFO

Article history:
Received 9 August 2014
Received in revised form 21 May 2015
Accepted 25 May 2015
Available online 28 May 2015

Keywords:
Atomic layer deposition
Titanium dioxide
Porous silicon

ABSTRACT

TiO_2 thin films were grown on highly-doped p-Si (100) macro- and mesoporous structures by atomic layer deposition (ALD) using $TiCl_4$ and deionized water as precursors at 300 °C. The crystalline structure, chemical composition, and morphology of the deposited films and initial silicon nanostructures were investigated by scanning electron microscopy, transmission electron microscopy (TEM), energy dispersive X-ray spectroscopy, X-ray photoelectron spectroscopy, micro-Raman spectroscopy and X-ray diffraction (XRD). The mean size of TiO_2 crystallites was determined by TEM, XRD and Raman spectroscopy. It was shown that the mean crystallite size and the crystallinity of the TiO_2 are influenced dramatically by the morphology of the porous silicon, with the mesoporous silicon resulting in a much finer grain size and amorphous structure than the macroporous silicon having a partially crystal anatase phase. A simple model of the ALD layer growth inside the pores was presented.
© 2015 Elsevier B.V. All rights reserved.

1. Introduction

Dioxide titanium (TiO_2) is n-type semiconductor material of wide band gap ($E_g = 3–3.3$ eV) extensively used in different applications. TiO_2 is widely used in the synthesis of semiconductor photocatalysts [1,2], solar cell electrodes [3,4], and modern electronic optical devices [5,6]. Being a promising semiconductor material that is transparent to visible light and having excellent optical transmittance, TiO_2 films are also good materials for the development of microelectronics due to their high dielectric constant [7]. Recent interest has been paid by researchers to the nano-scale metal oxides, especially TiO_2, which has highly active surface area and demonstrates optical properties, induced by quantum-size effects, such as UV shift of absorption edge and room temperature photoluminescence [8].

There are a number of methods to deposit TiO_2 nanostructures (e.g. nanolayers, nanolaminates etc.): atomic layer deposition [9] (ALD), pulsed laser deposition [10], chemical beam epitaxy [11], sol–gel [12] etc. ALD is one of the most powerful methods for metal oxide layer fabrication. It does not depend on the substrate geometry and can be applied both for planar samples, 3D patterned substrates and porous media. This method allows controlling the thickness and varying the chemical composition of the deposited layers.

Porous silicon (PSi) is another material extensively used in different applications. Because of its unique physical properties, PSi has a large number of applications in optoelectronics [13,14], biotechnology [15,16], etc. The PSi structures also exhibit great potential in optical sensor applications due to the possible tuning of the active index used for detection of biological substances or chemical vapors [15,16].

It is expected that metal oxide (TiO_2) coatings of such nanostructures as PSi will form nanostructures possessing unique optical, structural and electrical properties that can be used for development of electrical/optical devices. Recent publications about the Li-ion battery anode material [17], biosensors [18], photovoltaics [19] and optical materials [20] confirm this expectation. Thus, TiO_2–nanosilicon structures are very promising for fabrication and improvement of various optical and electronic devices.

It is no doubt that the investigation of morphological features of such structures allows one to develop more stable and effective devices based on TiO_2–PSi. However, the main publications have been devoted to the ALD TiO_2 films on planar silicon substrates [21–23]. There is no information on how the morphology and chemical composition of initial nanosilicon will affect the structure of dioxide titanium. Recent articles devoted to this topic do not reveal morphological features of fabricated TiO_2 structures. Thus, such research is prospective rather than retrospective. The subject requires further investigation.

Here, we report the structural properties of ALD TiO_2 coated PSi surface. The surface morphology and phase structure of the ALD TiO_2 coated porous silicon were detected by scanning electron microscopy

* Corresponding author at: Adam Mickiewicz University NanoBioMedical Centre Umultowska 85 61-614 Poznan, Poland.
E-mail addresses: igoyat@amu.edu.pl, yatsunskiy@gmail.com (I. Iatsunskyi).

http://dx.doi.org/10.1016/j.tsf.2015.05.056
0040-6090/© 2015 Elsevier B.V. All rights reserved.

(SEM) and transmission electron microscopy (TEM), energy dispersive X-Ray spectroscopy (EDX), X-ray photoelectron spectroscopy (XPS), X-ray diffraction (XRD) and Raman spectroscopy. This study consisted of three stages: the first step was to explore the PSi structure; in the second step, we investigated the PSi–TiO_2 to figure out how the initial porous structure will affect the ALD TiO_2 morphology; and finally we examined the effect of the annealing process on the structures obtained. We revealed that the crystallinity of ALD TiO_2 layers strongly depends on the initial PSi structure, especially on the pore diameter. This discovery provides an understanding of morphology and phase evolution during ALD of porous materials. The results obtained are very promising for the improved use of PSi–TiO_2 structures in photocatalysts, photovoltaic and sensor application where it is important to tune their physical properties by the morphology of PSi–TiO_2.

2. Experimental details

2.1. Materials

Silicon wafers (<0.005 Ω cm resistivity, polished on the (100) face, B-doped) were obtained from Siegert Wafer GmbH. Other chemicals were purchased from Sigma-Aldrich Chemicals.

2.2. Porous silicon fabrication

The PSi samples were fabricated utilizing a metal-assisted chemical etching process (MACE) [24]. Silicon samples (1×1 cm), after standard RCA cleaning, were cleaned with acetone, isopropanol and deionized water via ultrasonic cleaning. A thin oxide layer was formed, and the surface became hydrophilic. This oxide layer was removed by dipping the samples in a dilute HF (5%) solution. The silver particles, which act as catalysts to assist the etching of silicon, were deposited on Si samples by immersion in 0.2 M HF and 10^{-4} M $AgNO_3$ metallization aqueous solutions. The time of immersion ranged from 30 s to 120 s. After the electroless metallization, two sets of samples were manufactured. The wafers were etched in aqueous solutions containing HF (40%), H_2O_2 (30%), and ultrapure H_2O at ratio concentration – 1) $H_2O_2/H_2O/HF$ = 80/80/20 – samples No. 1 – S1; 2) $H_2O_2/H_2O/HF$ = 15/80/40 – samples No. 2 – S2; for 60 min. After etching, the samples were etched in HNO_3 solution to remove the silver particles. After that, samples were dipped into HF (5%) to remove oxide and then were cleaned with deionized water and blown dry with nitrogen. The etching and immersion procedures were performed at room temperature.

2.3. Atomic layer deposition of the TiO_2 thin films

The samples of PSi were placed in the ALD reactor (Picosun). The TiO_2 thin films were deposited onto the PSi substrates using $TiCl_4$ and water as ALD precursors. Nitrogen (N_2) served both as a carrier and a purging gas. The $TiCl_4$ and water were evaporated at 20 °C. In this study, the standard cycle consisted of 0.1 s exposure to $TiCl_4$, 3 s N_2 purge, 0.1 s exposure to water and 4 s N_2 purge. The total flow rate of the N_2 was 150 sccm. The TiO_2 thin films were grown at temperature 300 °C. The number of deposition–purge cycles was 100 corresponding to approximately 7 nm of the TiO_2 film on the planar silicon surface. The growth rate was typically 0.5 Å/cycle for TiO_2 on the planar silicon surface. The growth per cycle (GPC) has been controlled by measuring the thickness of the film on Si-wafer reference substrates placed in the reactor. After TiO_2 deposition some samples were annealed at 400 °C for an hour in an ambient atmosphere.

2.4. Characterization

Several analysis and characterization techniques were employed to investigate PSi and ALD TiO_2 thin films. The surface morphology was investigated by SEM JEOL, JSM-7001F (operating voltage 15 kV) with an EDX analyzer (Oxford Instruments XMax 80 mm^2 detector). TEM images were obtained with a JEOL ARM 200F high-resolution transmission electron microscope (200 kV) with an EDX analyzer (JED2300, at least 30 accumulations, matrix 512×512 points in STEM mode). The cross-sections and lamellas for TEM investigations were prepared by Focused Ion Beam (FIB). The FIB milling was carried out with a JEOL, JIB-4000. A carbon thin film was first deposited to protect the area of interest from surface damage during the FIB milling and then the Ga^+ beam with different acceleration voltages (5–30 kV) was used to prepare lamellae. Surface structural and chemical properties of the PSi and ALD TiO_2 thin films were analyzed by means of the XPS technique mounted within the Omicron Nanotechnology multiprobe UHV system, using a monochromatized Al-Kα X-ray as the excitation source ($h\nu$ = 1486.6 eV) and choosing C 1s (284.8 eV) as the reference line. XPS was conducted under ultrahigh vacuum (10^{-7} Pa). CasaXPS software was used to analyze the XPS data. XRD data (theta/2 theta mode) were collected using an Empyrean diffractometer using a copper X-ray source operating at 30 mA and 40 kV providing K_α radiation at a wavelength of 1.5408 Å. XRD data were collected in the range 20° to 80° 2θ with a step size of 0.013°. Raman scattering measurements were performed using a Renishaw micro-Raman spectrometer equipped with a confocal microscope (Leica). The samples were measured in backscattering geometry with a spectral resolution better than 1.0 cm^{-1}. The incident light was not polarized and also the light detector contained no polarization filters. The Raman scattering spectra were excited by a 514 nm laser. The beam was focused on the samples with a 50× microscope objective with a numerical aperture of 0.4. The incident optical power was changed by using neutral density filters in the beam path.

3. Results and discussion

Typical plan-view SEM images of PSi and PSi–TiO_2 are shown in Fig. 1a, b, d and e. The morphology of the PSi layer obtained by the MACE is quite different for sample 1 – S1 (Fig. 1a) and sample 2 – S2 (Fig. 1d). The PSi layer consists of a large number of small pores for S2 – mesoporous-Si (meso-PSi) structure (Fig. 1d), compared to S1, where one can see the macroporous Si (macro-PSi) structure. The macro-PSi layers exhibit the matt and dark surface, whereas the meso-PSi (Fig. 1d) films have a homogeneous interface and mirror-like surface. The mean pore size is less than 10 nm for meso-PSi (S2) and is more than 50 nm for macro-PSi (S1). The cross-sectional SEM view of the same sample shows the presence of large pores propagating into the bulk from the surface in a perpendicular manner for S1 and in a random manner for S2 (not shown here).

Cross-sectional SEM and TEM images indicate that the ALD TiO_2 layer infiltrates and coats the pores conformally for both samples. The EDX mapping image showing the distribution of Si, Ti and O atoms in the macro-PSi layer is presented in Fig. 1c. The EDX mapping image confirms that the Ti and O atoms penetrate quite uniformly into the macro-PSi matrix. Opposite to the deposition of films on flat surfaces, the precursor molecules have to diffuse into the porous structure. During the ALD process, molecules of precursors penetrate into the pore forming the layer or other structures of TiO_2 inside the PSi matrix. High-resolution TEM image shows the appearance of some crystallites in the PSi matrix (Fig. 1f). Lattice fringes are clearly visible, which proves the crystallinity of particles obtained. We determined the fringe separation of 0.35 nm and 0.27 nm for anatase and silicon respectively. They correspond to the lattice distance of (101) and (002) planes of the anatase and silicon. Diffraction measurements (shown later) also indicate only spacings due to anatase and silicon with no preferred orientation of crystallites. The mean crystallite size is approximately 7 ± 2 nm before and 9 ± 2 nm after annealing. The particle sizes of S1 determined from the TEM images are in good agreement with the values obtained by applying the Scherrer equation to the XRD patterns (shown later). For meso-PSi samples we did not observe crystallites inside the porous Si matrix which indicates the existence of amorphous phase of TiO_2.

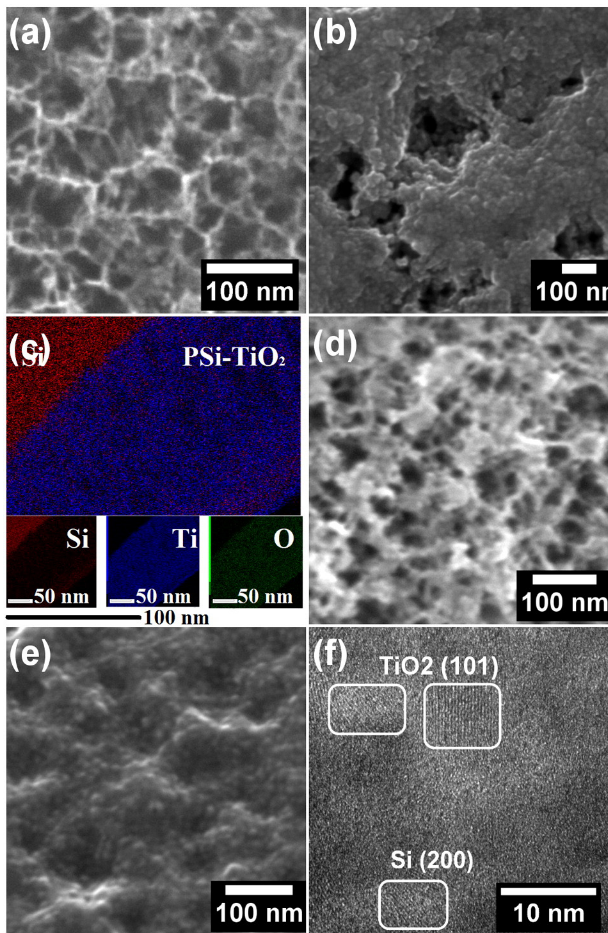

Fig. 1. (a) Macro-PSi surface, (b) macro-PSi surface after 150 ALD cycles, (c) cross-sectional EDX elemental mapping of the macro-PSi layer after 150 ALD cycles, (d) meso-PSi surface, (e) meso-PSi surface after 150 ALD cycles, and (f) HRTEM cross-sectional image of the macro-PSi after 150 ALD cycles.

XPS measurements were performed to determine the chemical composition of ALD TiO_2 films deposited on PSi. The results of these measurements are presented in Fig. 2. Survey spectra of meso-PSi surface after 100 ALD cycles indicate the appearance of many peaks (at 7.2 eV, 22.3 eV, 37.5 eV, 62.6 eV, 100.6 eV, 152 eV, 285 eV, 460 eV, 530 eV, 564 eV, 689 eV, 975 eV and 1072 eV), which represent the binding energies of O 2p, O 2s, Ti 3p, Ti 3s,si 2p,si 2s, C 1s, Ti 2p, O 1s, Ti 2s, F 1s, O KLL and Ti LMM respectively (Fig. 2a). Fig. 2b shows the Ti 2p spectrum. The appearance of two peaks at 464.4 eV and 458.7 eV were assigned to Ti $2p_{1/2}$ and Ti $2p_{3/2}$ respectively. The measured spin-orbit splitting is 5.7 eV, which indicates a valence state of +4 for Ti [25]. These results indicate that the product after the ALD process is TiO_2. After curve fitting, three peaks are observed for O 1s spectra (Fig. 2c) at 532.6 eV, 531.4 eV and 530.1 eV, which correspond to the binding energies of dioxide silicon (O–Si–O), hydroxyl group (Ti–OH) and Ti–O bonds (TiO_2), respectively. The difference between the binding energies of the assigned hydroxyl (531.4 eV) and titanium dioxide (530.1) is 1.3 eV, which is close to the previously reported value [25]. It appears that the peak at 532.6 eV corresponds to Si–O–Ti bonds as shown by Rungthiwa Methaapanon and Stacey F. Bent [26]. The authors of this publication showed that the interface between the SiO_2 and TiO_2 is abrupt and composed of Si–O–Ti bonds. The XPS results we obtained for macro-PSi are similar to meso-PSi samples, which indicate the formation of titanium oxide for both samples, regardless of the PSi structure.

In order to obtain further information on the structure and the phase of the samples, X-ray analysis was carried out. Fig. 3 shows the XRD of meso-PSi and meso-PSi-TiO_2 before and after annealing. We can observe a large number of secondary X-ray peaks of Si ((111), (330), (200) etc.) indicating a polycrystalline structure of the surface containing very small and disoriented crystallites [27]. The X-ray diffraction from the meso-PSi- TiO_2 does not display any peaks of TiO_2 on the

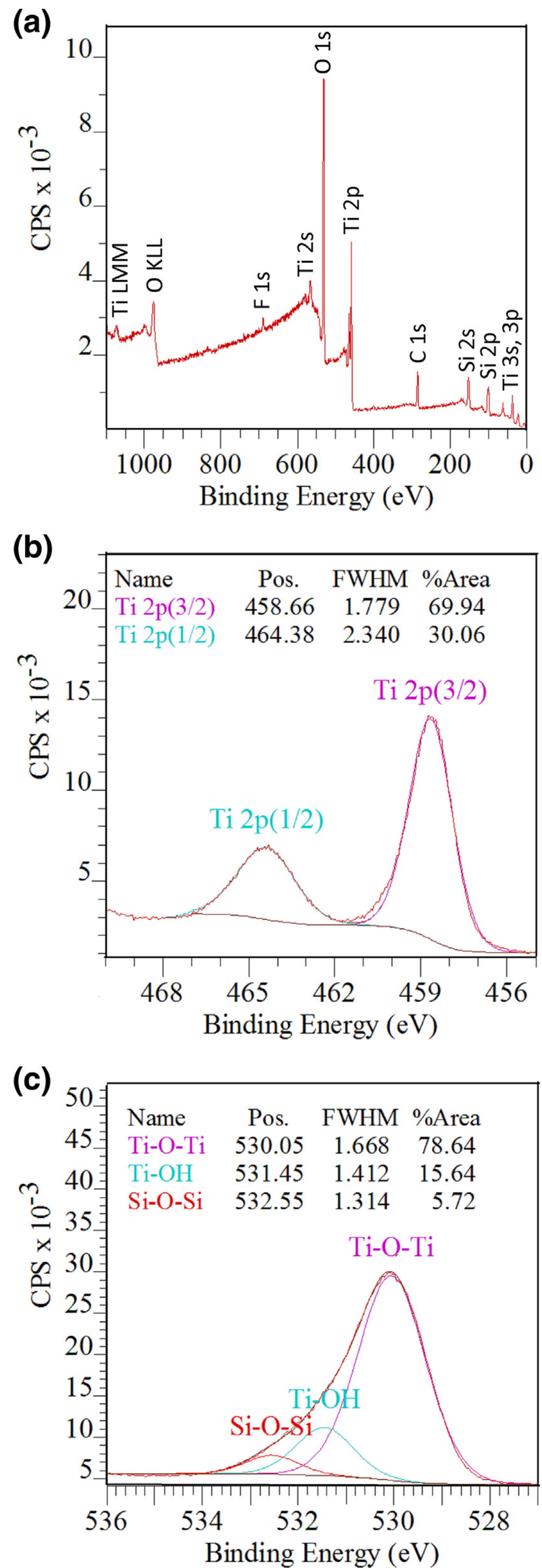

Fig. 2. (a) Survey XPS spectrum of the meso-PSi-TiO_2 (100 ALD cycles), (b) detailed high-resolution XPS spectra of the Ti 2p peak and (c) O 1s peak.

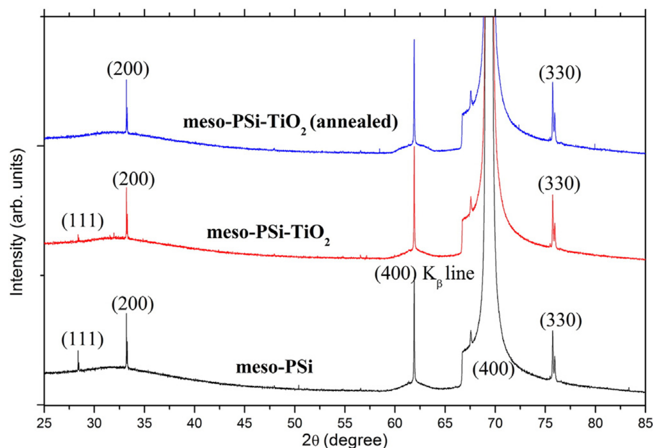

Fig. 3. XRD patterns of the as-prepared meso-PSi and meso-PSi-TiO_2 (150 ALD cycles) before and after annealing.

diffuse scattering background, indicating that amorphous TiO_2 films were likely obtained for this sample.

Fig. 4 shows XRD patterns of the macro-PSi-TiO_2 before and after annealing. The XRD peak at 33° of the sample was assigned to the (200) plane of Si. According to Fig. 4, the strongest peak at (200) was greatly reduced after deposition and further annealing when compared with that of PSi. This may be explained by considering that the surface of PSi is packed with titanium dioxide. A small XRD peak at $2\theta = 25.4°$ corresponding to (101) reflections of TiO_2 (anatase phase) appears after ALD deposition. The intensity of the anatase XRD peak becomes stronger after annealing. This might be caused by the amorphous–crystalline phase transition. The mean size of TiO_2 nanocrystallite was determined from the full width at half maximum (FWHM) of the XRD peaks using the Scherrer equation:

$$D = \frac{0.9\ \lambda}{FWHM\ \ \cos\theta}; \quad (1)$$

where D and λ mean the nanocrystallite size and X-ray wavelength, respectively. The mean size of TiO_2 nanocrystallite inside the macro-PSi matrix was 9.3 ± 2 nm.

In order to determine the crystallinity of obtained layers we also used Raman spectroscopy as very sensitive local method. Fig. 5a shows the Raman spectrum of the TiO_2 nanocrystalline film on macro-PSi before and after annealing. Besides one and two-phonon silicon peaks at 300 cm^{-1} ($2TA_x$ – two-phonon transverse acoustic mode),

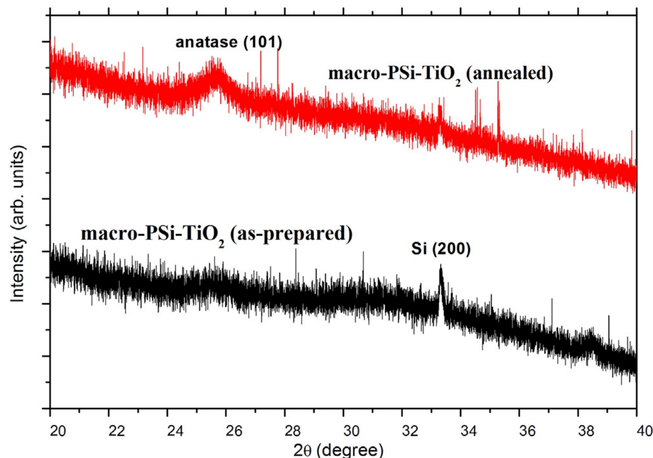

Fig. 4. XRD pattern for the TiO_2 film deposited onto macro-PSi before and after annealing. XRD patterns were confirmed with the JCPDS file No. 21-1272.

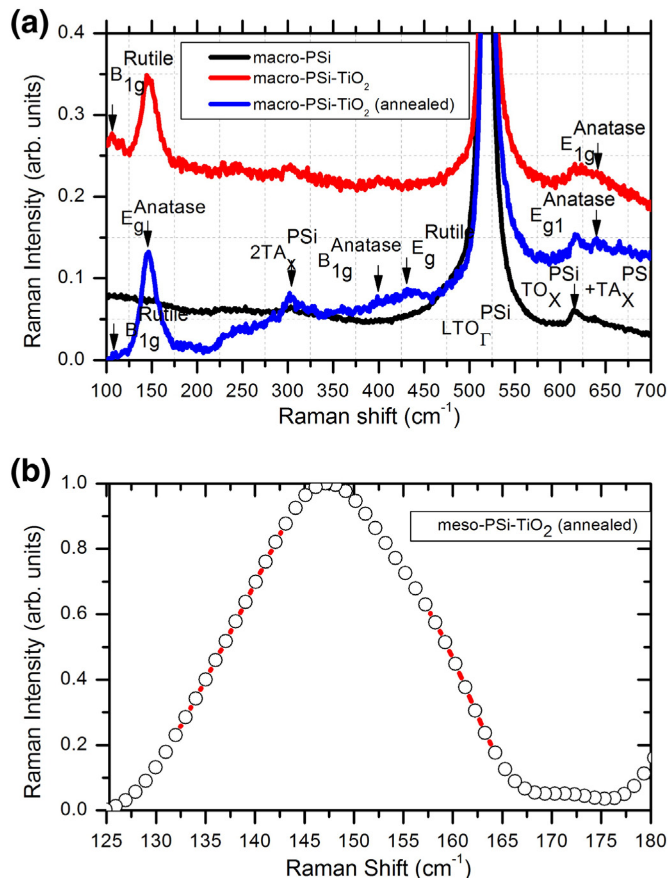

Fig. 5. (a) Raman spectrum of the macro-PSi and TiO_2 films deposited onto macro-PSi before and after annealing; (b) the E_g peak of anatase for the annealed meso-PSi-TiO_2 (black circles – experimental data, red line – simulated curve). For interpretation of the references to color in this figure legend, the reader is referred to the web version of this article.

520 cm^{-1} (LTO_Γ – first-order Raman optical mode), and 610 cm^{-1} ($TO_x + TA_x$ – two-phonon transverse acoustic and optical mode) [28], the Raman lines at 145, 410 and 630 cm^{-1} can be assigned as the E_g, B_{1g} and E_g modes of the anatase phase, respectively [29–32]. These peaks are similar to those in the bulk anatase with the exception of their frequency blueshift and FWHM increase [30–32]. The strongest E_g mode at 144 cm^{-1} arising from the external vibration of the anatase structure is well resolved. The measured Raman spectrum shows that the as-prepared TiO_2 layer is partially crystallized in the anatase structure. This conclusion is consistent with the XRD and TEM results shown in Figs. 4 and 1f.

There are also small peaks at 105 cm^{-1} and at 400 cm^{-1} probably corresponding to the B_{1g} and E_g modes of the rutile phase, respectively. After annealing these peaks become slightly higher. It is suggested here that a partial transformation anatase–rutile phase might occur. However, it has been reported that no structural transformation to other crystalline phases of ALD TiO_2 occurs for temperatures up to 700 °C [29]. Thus, more likely these peaks can be attributed to some other modes of nanosilicon. Regarding meso-PSi-TiO_2, the broad peak at 150 cm^{-1} indicates the presence of an amorphous anatase phase (Fig. 5b) before and after annealing.

A simple confinement model has been used to calculate the shape of the 144 cm^{-1} mode of the anatase at various nanocrystal sizes, and to determine the average size of nanocrystallites. The Raman spectrum is given by [30]:

$$I(\omega) = \int_{BZ} \frac{d^3q\ |C(0,q)|^2}{(\omega - \omega(q))^2 - \left(\frac{\Gamma_0}{2}\right)^2} \quad (2)$$

Table 1
Mean crystallite size of TiO_2 crystallites.

Sample	TEM [nm]	XRD [nm]	Raman [nm]
S1	7 ± 2	–	4.5 ± 1.5
S1 (annealed)	9 ± 2	9.3 ± 2	6 ± 1.5
S2	–	–	<4
S2 (annealed)	–	–	<4

where

$$|C(0,q)|^2 = \exp\left(-\frac{q^2L^2}{16\pi^2}\right) \tag{3}$$

The first-order Raman spectrum $I(\omega)$ is thus given by:

$$I(\omega) = \int_{BZ} \frac{4\pi q^2 \exp\left(-\frac{q^2L^2}{16\pi^2}\right) d^3q}{(\omega - \omega(q))^2 - \left(\frac{\Gamma_0}{2}\right)^2} \tag{4}$$

where Γ_0 is the Raman linewidth at room temperature, and $\omega(q)$ is the phonon dispersion curve. The broadening and the shift of a Raman peak are a result of this integration. For the 144 cm^{-1} mode of the anatase, we used $\Gamma_0 = 7$ cm^{-1} obtained from the data in [31]. The dispersion curve used for the anatase is:

$$\omega = \omega_0 + \Delta[1 - \cos(q \cdot a)] \tag{5}$$

where ω_0 – maximum peak position, $\Delta = 20$ cm^{-1} and $a = 0.3768$ nm. The nanocrystallite size of TiO_2 in macro-PSi was estimated to be 4.5 ± 1.5 nm before and 6 ± 1.5 nm after annealing. In the case of meso-PSi, when the size is less than 4 nm, the model cannot be used, as details of the dispersion curve and of the shape of the Brillouin zone become critical [30].

Summarizing the results of SEM, TEM, XRD and Raman spectroscopy we present the data of the average size of the TiO_2 nanocrystallites as Table 1. We can conclude that for the macro-PSi sample only, the layer of TiO_2 has a crystal anatase phase before and after annealing. This conclusion arises from the data of the electron microscopy, X-ray and Raman studies. It is obvious there is some distribution of the mean crystallite size not only along the surface, but also in the PSi layer. This was concluded taking into account that the penetration depth (PD) of the laser spot in the Raman spectroscopy must differ from the X-ray beam PD. Therefore, the mean crystallite size obtained from Raman spectroscopy and XRD differs. A complex relationship emerges as many factors are involved. Furthermore, in the present calculations of the crystallite size, neither the mechanical stresses, nor non-stoichiometry influences have been considered [32]. However, it is no doubt that the mean crystallite size and the crystallinity of dioxide titanium are influenced dramatically by the morphology of the PSi, with the meso-PSi resulting in a much smaller crystallite size and amorphous structure than to macro-PSi having a partially crystal anatase phase.

To better understand the reasons for this, we propose a simple model of the ALD process of the PSi. The initial stage of film growth involves the formation of an amorphous layer, which subsequently crystallizes. As shown in many publications [21–23,33], crystallization of the amorphous film occurs at some point between 100 and 200 cycles. At 300 °C approximately 100 cycles are required to initiate crystallization [34]. Both the temperature and the growth stress play significant roles in the crystallization process. Mitchel et al. [34,35] have shown that the onset of crystallization is controlled even more by compressive stress in the films than the time of annealing. The stresses in the ALD TiO_2 films are compressive and increase with thickness.

Based on the experimental results, we can suggest a model to describe the ALD film growth inside the porous media. In the case of a plane surface, the film grows vertically and after approximately 100 cycles the crystallization is initiated due to sufficient values of temperature and compressive stress. In the case of PSi, the layers of TiO_2 start to grow horizontally along the pore wall (Fig. 6). Depending on the diameter of the pore, the layers of TiO_2 first grow towards each other and then may fit closely. Taking into account the value of GPC = 0.5 Å/cycle, we hypothesize the growth of ALD film inside the pore as a deposition of 0.5 Å layer per cycle. The inner diameter of the pore is reduced by 1 Å every ALD cycle. The pore having a diameter of less than 10 nm, like a meso-PSi, would be completely filled by TiO_2 before approximately 100 ALD cycles, therefore, TiO_2 has an amorphous structure. In the case of a macroporous structure, especially if the diameter of the pore is over 50 nm, it is possible that a parallel film consisting of more than 100 ALD layers grows inside the pore, i.e. after 100 cycles. As a consequence, the crystallization of TiO_2 occurs inside the pore.

4. Conclusion

ALD TiO_2 thin films grown on macro- and meso-PSi surface have been investigated by means of electron microscopy, XPS, EDX, micro-Raman spectroscopy and XRD. The crystalline structure, chemical composition, and morphology of the deposited films and initial PSi were established. The approximate size of TiO_2 nanocrystals was estimated using TEM, XRD and Raman spectroscopy. The results presented above, demonstrate that the morphology of TiO_2 films deposited by ALD strongly depends on the initial PSi structure. It was shown that

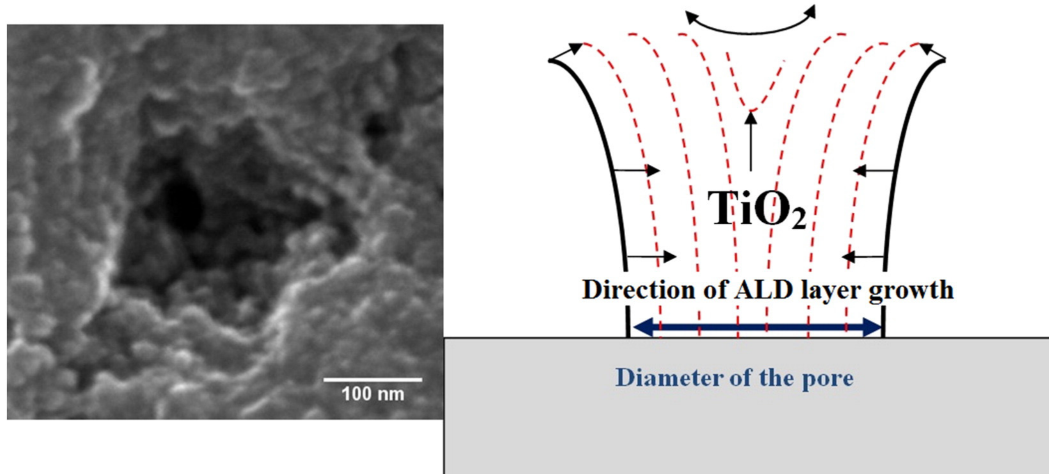

Fig. 6. The scheme of the "closing" of the opposite TiO_2 layers. Arrows indicate the direction of the titanium oxide film growth. Left SEM image – top view of single pore after 150 ALD cycles.

the mean crystallite size and the crystallinity of the dioxide titanium are strongly influenced by the morphology of the PSi, with the meso-PSi resulting in a much finer grain size and amorphous structure than to macro-PSi having partially crystal anatase phase. A simple model of the ALD coating in the porous media was presented. Taking into account that minimum 100 cycles are required to initiate crystallization of amorphous film, we conclude that the numbers of ALD cycles (i.e. parallel monolayers) are restricted by the pore diameter.

Acknowledgment

Financial support from the National Centre for Research and Development under research grant “Nanomaterials and their application to biomedicine”, contract number PBS1/A9/13/2012 is gratefully acknowledged.

References

[1] A. Fujishima, K. Honda, Electrochemical Photolysis of Water at a Semiconductor Electrode, Nature 238 (1972) 37.
[2] D.C. Hurum, A.G. Agrios, K.A. Gray, T. Rajh, M.C. Thurnauer, Explaining the Enhanced Photocatalytic Activity of Degussa P25 Mixed-Phase TiO_2 Using EPR, J. Phys. Chem. B 107 (2003) 4545.
[3] W. Qin, S. Lu, X. Wu, S. Wang, Dye-sensitized Solar Cell Based on N-Doped TiO_2 Electrodes Prepared on Titanium, Int. J. Electrochem. Sci. 8 (2013) 7984.
[4] A. Sedghi, H. Nourmohammadi Miankushki, Influence of TiO_2 Electrode Properties on Performance of Dye Sensitized Solar Cells, Int. J. Electrochem. Sci. 7 (2012) 12078.
[5] T. Touam, L. Znaidi, D. Vrel, I. Ninova-Kuznetsova, O. Brinza, A. Fischer, A. Boudrioua, Low Loss Sol-Gel TiO_2 Thin Films for Waveguiding Applications, Coatings 3 (2013) 49.
[6] A. Herman Yuwono, J. Xue, J. Wang, H. Izaac Elim, W. Ji, Transparent nanohybrids of nanocrystalline TiO_2 in PMMA with unique nonlinear optical behavior, J. Mater. Chem. 13 (2003) 1475.
[7] S.A. Campbell, D.C. Gilmer, Xiao-Chuan Wang, Ming-Ta Hsieh, Hyeon-Seag Kim, W.L. Gladfelter, MOSFET transistors fabricated with high permitivity TiO_2 dielectrics, IEEE Trans. Electron Devices 44 (1997) 104.
[8] A.A. Chaaya, R. Viter, M. Bechelany, Z. Alute, D. Erts, A. Zalesskaya, K. Kovalevskis, V. Rouessac, V. Smyntyna, P. Miele, Evolution of microstructure and related optical properties of ZnO grown by atomic layer deposition, Beilstein J. Nanotechnol. 4 (2013) 690.
[9] T. Nam, Jae-Min Kim, Min-Kyu Kim, Hyungjun Kim, Low-temperature Atomic Layer Deposition of TiO_2, Al_2O_3, and ZnO Thin Films, J. Korean Phys. Soc. 59 (2011) 452.
[10] P. Kuppusami, N. Parvathavarthini, E. Mohandas, Pulsed laser deposition of anatase and rutile TiO_2 thin films, Surf. Coat. Technol. 201 (2007) 713.
[11] A. Lotnyk, S. Senz, D. Hesse, Epitaxial growth of TiO_2 thin films on $SrTiO_3$, $LaAlO_3$ and yttria-stabilized zirconia substrates by electron beam evaporation, Thin Solid Films 515 (2007) 3439.
[12] P. Kajitvichyanukula, J. Ananpattarachaia, S. Pongpom, Sol–gel preparation and properties study of TiO_2 thin film for photocatalytic reduction of chromium(VI) in photocatalysis process, Sci. Technol. Adv. Mater. 6 (2005) 352.
[13] E.C. Garnett, P. Yang, Silicon Nanowire Radial p-n Junction Solar Cells, J. Am. Chem. Soc. 130 (2008) 9224.
[14] P. Bettotti, L. Pavesi, Nanosilicon: a new platform for photonics, Phys. Status Solidi C 8 (2011) 2880.
[15] S. Dhanekar, S. Jain, Porous silicon biosensor: Current status, Biosens. Bioelectron. 41 (2013) 54.
[16] T. Karacali, U. Cem Hasar, I. Yucel Ozbek, E. Argun Oral, H. Efeoglu, Novel Design of Porous Silicon Based Sensor for Reliable and Feasible Chemical Gas Vapor Detection, J. Lightwave Technol. 31 (2013) 295.
[17] E. Memarzadeh Lotfabad, P. Kalisvaart, Kai Cui, A. Kohandehghan, M. Kupsta, B. Olsena, D. Mitlin, ALD TiO_2 coated silicon nanowires for lithium ion battery anodes with enhanced cycling stability and coulombic efficiency, Phys. Chem. Chem. Phys. 15 (2013) 13646.
[18] J. Li, M.J. Sailor, Synthesis and characterization of a stable, label-free optical biosensor from TiO_2-coated porous silicon, Biosens. Bioelectron. 55 (2014) 372.
[19] S. Avasthi, W.E. McClain, G. Man, A. Kahn, J. Schwartz, J.C. Sturm, Hole-blocking titanium-oxide/silicon heterojunction and its application to photovoltaics, Appl. Phys. Lett. 102 (2013) 203901.
[20] I. Iatsunskyi, M. Pavlenko, R. Viter, M. Jancelewicz, G. Nowaczyk, I. Baleviciute, K. Załęski, S. Jurga, A. Ramanavicius, V. Smyntyna, Tailoring the structural, optical, and photoluminescence properties of porous silicon/TiO_2 nanostructures, J. Phys. Chem. C 119 (2015) 7164.
[21] J. Shi, Z. Li, A. Kvit, S. Krylyuk, A.V. Davydov, X. Wang, Electron Microscopy Observation of TiO_2 Nanocrystal Evolution in High-Temperature Atomic Layer Deposition, Nano Lett. 13 (2013) 5727.
[22] S. McDonnell, R.C. Longo, O. Seitz, J.B. Ballard, G. Mordi, D. Dick, J.H.G. Owen, J.N. Randall, J. Kim, Y.J. Chabal, K. Cho, R.M. Wallace, Controlling the Atomic Layer Deposition of Titanium Dioxide on Silicon: Dependence on Surface Termination, J. Phys. Chem. C 117 (2013) 20250.
[23] Y. Huang, G. Pandraud, P.M. Sarro, Characterization of low temperature deposited atomic layer deposition TiO_2 for MEMS applications, J. Vac. Sci. Technol. A 31 (2013) 01A148.
[24] Z. Huang, N. Geyer, P. Werner, J. de Boor, U. Gösele, Metal-Assisted Chemical Etching of Silicon: A Review, Adv. Mater. 23 (2011) 285.
[25] C. Rath, P. Mohanty, A.C. Pandey, N.C. Mishra, Oxygen vacancy induced structural phase transformation in TiO_2 nanoparticles, J. Phys. D. Appl. Phys. 42 (2009) 205101.
[26] R. Methaapanon, S.F. Bent, Comparative Study of Titanium Dioxide Atomic Layer Deposition on Silicon Dioxide and Hydrogen-Terminated Silicon, J. Phys. Chem. C 114 (2010) 10498.
[27] D. Bellet, G. Dolino, X-Ray diffraction of Porous silicon, Thin Solid Films 276 (1996) 1.
[28] H. Tanino, A. Kuprin, H. Deai, Raman study of free-standing porous silicon, Phys. Rev. B 53 (4) (1996) 1937.
[29] A. Niilisk, M. Moppel, M. Pears, I. Sildos, T. Jantson, T. Avarmaa, R. Jaaniso, J. Aarik, Structural study of TiO_2 thin films by micro-Raman spectroscopy, Cent. Eur. J. Phys. 4 (2006) 105.
[30] Ke-Rong Zhu, Ming-Sheng Zhang, Qiang Chen, Zhen Yin, Size and phonon-confinement effects on low-frequency Raman mode of anatase TiO_2 nanocrystal, Phys. Lett. A 340 (2005) 220.
[31] D. Bersani, P.P. Lottici, Xing-Zhao Ding, Phonon confinement effects in the Raman scattering by TiO_2 nanocrystals, Appl. Phys. Lett. 72 (1998) 73.
[32] W.F. Zhang, Y.L. He, M.S. Zhang, Z. Yin, Q. Chen, Raman scattering study on anatase TiO_2 nanocrystals, J. Phys. D. Appl. Phys. 33 (2000) 912.
[33] J. Aarik, A. Aidla, T. Uustare, V. Sammelseig, Morphology and structure of TiO_2 thin films grown by atomic layer deposition, J. Cryst. Growth 148 (1995) 268.
[34] D.R.G. Mitchell, D.J. Attard, G. Triani, Transmission electron microscopy studies of atomic layer deposition TiO_2 films grown on silicon, Thin Solid Films 441 (2003) 85.
[35] D.R.G. Mitchell, G. Triani, D.J. Attard, K.S. Finnie, P.J. Evans, C.J. Barb´e, J.R. Bartlett, Atomic layer deposition of TiO_2 and Al_2O_3 thin films and nanolaminates, Smart Mater. Struct. 15 (2006) S57.